

## IMPROVED CONSTRAINTS ON PRIMORDIAL NON-GAUSSIANITY FOR THE WILKINSON MICROWAVE ANISOTROPY PROBE 5-YR DATA

A. CURTO<sup>1</sup>, E. MARTÍNEZ-GONZÁLEZ AND R. B. BARREIRO  
IFCA, CSIC-Univ. de Cantabria, Avda. los Castros, s/n, E-39005-Santander, Spain  
*Draft version November 18, 2018*

### ABSTRACT

We present constraints on the non-linear coupling parameter  $f_{nl}$  with the Wilkinson Microwave Anisotropy Probe (WMAP) data. We use an updated method based on the spherical Mexican hat wavelet (SMHW) which provides improved constraints on the  $f_{nl}$  parameter. This paper is a continuation of a previous work by Curto et al. where several third order statistics based on the SMHW were considered. In this paper, we use all the possible third order statistics computed from the wavelet coefficient maps evaluated at 12 angular scales. The scales are logarithmically distributed from 6.9 arcmin to 500 arcmin. Our analysis indicates that  $f_{nl}$  is constrained to  $-18 < f_{nl} < +80$  at 95% confidence level (CL) for the combined V+W WMAP map. This value has been corrected by the presence of undetected point sources, which adds a positive contribution of  $\Delta f_{nl} = 6 \pm 5$ . Our result excludes at  $\sim 99\%$  CL the best-fitting value  $f_{nl} = 87$  reported by Yadav & Wandelt. We have also constrained  $f_{nl}$  for the Q, V and W frequency bands separately, finding compatibility with zero at 95 % CL for the Q and V bands but not for the W band. We have performed some further tests to understand the cause of this deviation which indicate that systematics associated to the W radiometers could be responsible for this result. Finally we have performed a Galactic North-South analysis for  $f_{nl}$ . We have not found any asymmetry, i.e. the best-fitting  $f_{nl}$  for the northern pixels is compatible with the best-fitting  $f_{nl}$  for the southern pixels.

*Subject headings:* methods: data analysis – cosmic microwave background

### 1. INTRODUCTION

The cosmic microwave background (CMB) offers a picture of the early Universe when it was only 400,000 years old. The CMB photons last scattered off electrons at that time and since then they traveled free through the space. The primordial perturbations set up during inflation are imprinted in both radiation and matter distribution. The CMB temperature anisotropies, related with the primordial perturbations, can be used to test some assumptions of the so called standard model. In particular, we can test the prediction of the standard, single field, slow roll inflation (Guth 1981; Albrecht & Steinhardt 1982; Linde 1982, 1983) which states that the anisotropies are compatible with a nearly Gaussian random field. Other non-standard models of inflation predict detectable levels of non-Gaussianity in the anisotropies (see e.g. Bartolo et al. 2004).

Primordial non-Gaussianity of the local form is characterised by the non-linear coupling parameter  $f_{nl}$  (Salopek & Bond 1990; Gangui et al. 1994; Verde et al. 2000; Komatsu & Spergel 2001):

$$\Phi(\mathbf{x}) = \Phi_L(\mathbf{x}) + f_{nl} \{ \Phi_L^2(\mathbf{x}) - \langle \Phi_L^2(\mathbf{x}) \rangle \} \quad (1)$$

where  $\Phi(\mathbf{x})$  is the primordial gravitational potential and  $\Phi_L(\mathbf{x})$  is a linear random field which is Gaussian distributed and has zero mean.

There are many studies based on different statistical tools to constrain the local  $f_{nl}$  parameter from the CMB anisotropies, using the data of different experiments. We can mention the analyses using

the angular bispectrum and wavelets on the Cosmic Background Explorer (COBE) data (Komatsu et al. 2002; Cayón et al. 2003), the angular bispectrum on MAXIMA data (Santos et al. 2003), the angular bispectrum on WMAP data (Komatsu et al. 2003; Creminelli et al. 2006, 2007; Spergel et al. 2007; Yadav & Wandelt 2008; Komatsu et al. 2009; Smith et al. 2009), different kind of wavelet analyses on WMAP data (Mukherjee & Wang 2004; Cabella et al. 2005; Curto et al. 2009), the Minkowski functionals on BOOMERanG data (De Troia et al. 2007), the Minkowski functionals on Archeops data (Curto et al. 2007, 2008), the Minkowski functionals on WMAP data (Komatsu et al. 2003; Spergel et al. 2007; Gott et al. 2007; Hikage et al. 2008; Komatsu et al. 2009) among others. We can also mention new promising techniques as for example one based on the  $n$ -point probability density distribution (Vielva & Sanz 2009), and other based on needlets (Pietrobon et al. 2009; Rudjord et al. 2009). Other works are based on the use of the large scale structure to constrain  $f_{nl}$  (Slosar et al. 2008).

This work is a continuation of the wavelet-based analysis by Curto et al. (2009) of the WMAP<sup>2</sup> data. We use high resolution WMAP data maps, and compute the wavelet coefficients for 12 angular scales logarithmically spaced from 6.9 arcmin to 500 arcmin. With these wavelet coefficients we compute all the possible third order moments involving these scales.

The article is organised as follows. Section 2 presents the estimators used to test Gaussianity and to constrain  $f_{nl}$ , the data maps and the simulations. Section 3 summarises the main results of this work and the conclusions

Electronic address: curto@ifca.unican.es

<sup>1</sup> Also at Dpto. de Física Moderna, Univ. de Cantabria, Avda. los Castros, s/n, 39005-Santander, Spain

<sup>2</sup> <http://map.gsfc.nasa.gov/>

are in Section 4.

## 2. METHODOLOGY

This analysis is based on the spherical Mexican hat wavelet (SMHW) as defined in Martínez-González et al. (2002). For references about the use of the SMHW to test Gaussianity in the CMB see for example the review by Martínez-González (2008). We compute the wavelet coefficient maps at several scales  $R_i$  logarithmically separated ( $R_{i+1}/R_i$  constant). The considered scales are<sup>3</sup>:  $R_1 = 6.9'$ ,  $R_2 = 10.6'$ ,  $R_3 = 16.3'$ ,  $R_4 = 24.9'$ ,  $R_5 = 38.3'$ ,  $R_6 = 58.7'$ ,  $R_7 = 90.1'$ ,  $R_8 = 138.3'$ ,  $R_9 = 212.3'$ ,  $R_{10} = 325.8'$ ,  $R_{11} = 500'$ . We also include the unconvolved map, which will be represented by the scale  $R_0$  as in Curto et al. (2009). For each possible combination of three scales  $R_i$ ,  $R_j$ , and  $R_k$  (where the indices  $i$ ,  $j$ , and  $k$  can be repeated) we define a third order statistic

$$q_{ijk} = \frac{1}{N_{i,j,k}} \sum_{p=0}^{N_{pix}-1} \frac{w_{p,i}w_{p,j}w_{p,k}}{\sigma_i\sigma_j\sigma_k} \quad (2)$$

where  $N_{pix}$  is the total number of pixels of the map,  $N_{i,j,k}$  is the number of pixels available after combining the extended masks corresponding to the three scales  $R_i$ ,  $R_j$  and  $R_k$ ,  $w_{p,i} = w_p(R_i)$  is the wavelet coefficient in the pixel  $p$  evaluated at the scale  $R_i$ , and  $\sigma_i$  is the dispersion of  $w_{p,i}$ . Each map  $w_{p,i}$  is masked out with the corresponding extended mask at the scale  $R_i$  as in Curto et al. (2009). For a set of  $n$  scales we have  $n_{stat} = (n + 3 - 1)!/[3!(n - 1)!]$  third order statistics such as the one defined in Eq. (2). We have tested with simulations that these statistics have a Gaussian-like distribution. We can construct a vector  $\mathbf{q}$  of dimension  $n_{stat}$

$$\mathbf{q} = [q_{0,0,0}; q_{0,0,1}; \dots; q_{0,0,11}; q_{0,1,1}; \dots; q_{11,11,11}]. \quad (3)$$

With this vector we can perform two different analyses using a  $\chi^2$  statistic: one to test Gaussianity and a second one to constrain  $f_{nl}$  (Eqs. (7) and (8) of Curto et al. 2009).

We use the 5-yr WMAP foreground reduced data, available in the Legacy Archive for Microwave Background Data Analysis (LAMBDA) web site<sup>4</sup>. We combine the maps of different radiometers using the inverse of the noise variance as an optimal weight (Bennett et al. 2003). In particular we analyse the V+W, Q, V and W combined maps at a resolution of 6.9 arcmin, corresponding to a HEALPix (Górski et al. 2005)  $N_{side} = 512$ . We use the KQ75 mask and also a set of extended masks for the wavelet coefficient maps. We use the same masks as the ones described in Curto et al. (2009) for a threshold of 0.01. This corresponds to an available fraction of the sky from 71.2% for the  $R_1$  scale to 31.4% for the  $R_{11}$  scale. Notice that larger scales have the restriction of a lower available area, which means a lower sensitivity to  $f_{nl}$ .

Finally we analyse the data and compare them with Gaussian and non-Gaussian simulations. The Gaussian

<sup>3</sup> The level of discretisation of the wavelet space is a balance between the minimum number of scales needed to extract the non-Gaussian signal from the data and acceptable computational requirements.

<sup>4</sup> <http://lambda.gsfc.nasa.gov>

TABLE 1

$\chi^2$  CONSTRUCTED FROM THE 364 STATISTICS FOR V+W, Q, V, AND W DATA MAPS. WE ALSO PRESENT THE MEAN AND THE DISPERSION OF THE  $\chi^2$  CORRESPONDING TO 1,000 GAUSSIAN SIMULATIONS, AND THE CUMULATIVE PROBABILITY FOR THE  $\chi^2$  OF THE DATA OBTAINED FROM THE SIMULATIONS.

Map	$\chi^2_{data}$	DOF	$\langle \chi^2 \rangle$	$\sigma$	$P(\chi^2 \leq \chi^2_{data})$
V+W	349	364	379	49.2	0.29
Q	384	364	378	48.7	0.63
V	348	364	377	47.8	0.27
W	354	364	376	47.9	0.35

TABLE 2

BEST-FITTING  $f_{nl}$  VALUES OBTAINED FROM V+W, Q, V AND W COMBINED MAPS. WE ALSO PRESENT THE MEAN, DISPERSION AND SOME PERCENTILES OF THE DISTRIBUTION OF THE BEST FIT  $f_{nl}$  VALUES OBTAINED FROM GAUSSIAN SIMULATIONS.

Map	best $f_{nl}$	$\langle f_{nl} \rangle$	$\sigma(f_{nl})$	$X_{0.160}$	$X_{0.840}$	$X_{0.025}$	$X_{0.975}$
V+W	39	-1	25	-26	24	-51	47
Q	11	0	33	-31	34	-63	66
V	23	0	30	-28	30	-55	59
W	65	-4	30	-33	26	-59	58

simulations are performed using the best fit power spectrum  $C_\ell$  for WMAP provided by LAMBDA and the instrumental white noise of each WMAP radiometer. The non-Gaussian simulations with the  $f_{nl}$  contribution are computed following the algorithms described in Liguori et al. (2003, 2007) and transformed into WMAP maps with the instrumental noise included. We also estimate the unresolved point source contribution to  $f_{nl}$  for the V+W case by analysing point source simulations. These simulations have been generated as in Curto et al. (2009) following the source number counts  $dN/dS$  given by de Zotti et al. (2005).

## 3. RESULTS

In this Section we present the Gaussianity analysis of the WMAP data for the combined V+W, Q, V, and W data maps. We also constrain  $f_{nl}$  for these maps through a  $\chi^2$  test. We estimate the contribution of point sources to the V+W map. Finally we constrain  $f_{nl}$  for northern and southern pixels separately.

### 3.1. Analysis of WMAP data

We evaluate the wavelet coefficients at the 12 considered scales. With these coefficients we compute the third order estimators defined in Eq. (2). For 12 scales, we have 364 possible third order statistics. We compute these statistics for the data maps and for Gaussian simulations. The covariance matrix used in the  $\chi^2$  statistics is constructed from 10,000 Gaussian simulations. For the considered cases, V+W, Q, V and W, we have that the data are inside the  $2\sigma$  error bars, i.e., the data are compatible with Gaussian simulations. We compute a  $\chi^2$  statistic by comparing the data with the expected value of Gaussian simulations following Curto et al. (2009). We as well compute the  $\chi^2$  of an additional set of 1,000 Gaussian simulations. The  $\chi^2$  statistic of the data is compatible with the  $\chi^2$  of the Gaussian simulations. This is presented in Table 1.

We have studied the properties of the covariance matrix for the V+W map (see left panel of Fig. 1) which is

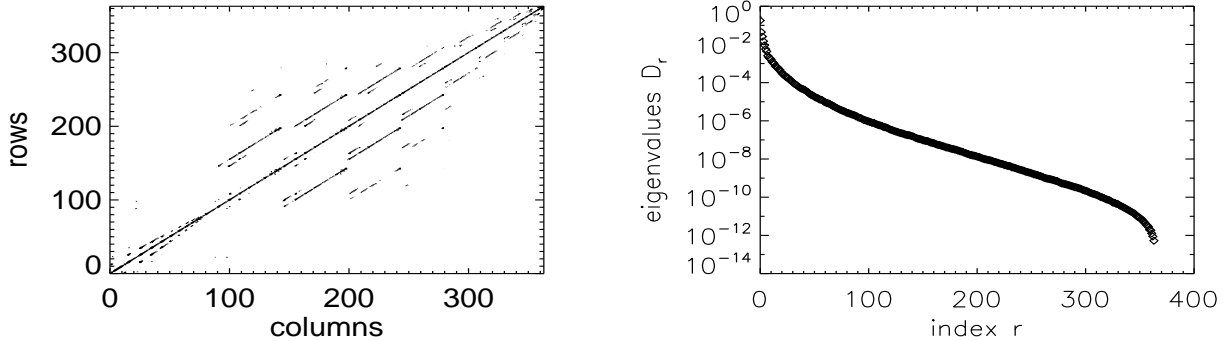


FIG. 1.— Left panel: the covariance matrix elements of the third order statistics for the V+W map that satisfy  $C_{ijk,rst}/\sqrt{C_{ijk,ijk}C_{rst,rst}} > 0.95$ . Right panel: the covariance matrix eigenvalues for the V+W map.

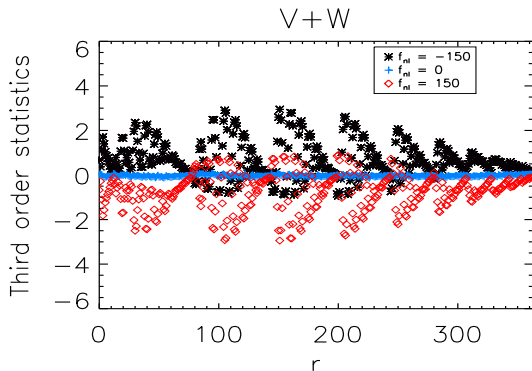


FIG. 2.— The expected values of the normalised third order statistics  $q_r$  for V+W simulations with different values of  $f_{nl}$ , where  $r \equiv \{i, j, k\}$  is ordered following Eq. (3).

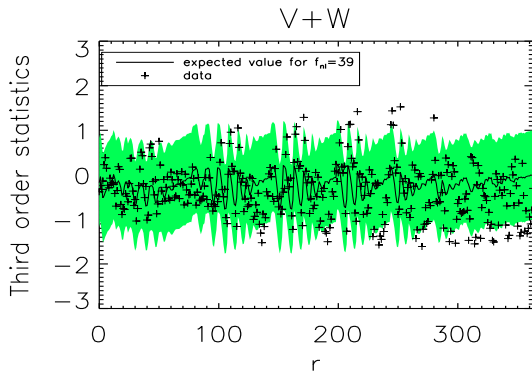


FIG. 3.— The normalised third order statistics  $q_r$  for the combined V+W data map. The solid line corresponds to the expected values for the best-fitting  $f_{nl}$  model ( $f_{nl} = 39$ ). We also plot the  $1\sigma$  error bars in green.

derived from 10,000 Gaussian simulations. We may wonder if that number of simulations is enough to achieve the convergence. The condition number, defined here as the ratio between the maximum and minimum eigenvalues (see right panel of Fig. 1) is  $Cond(C) \sim 10^{12}$ . An upper limit for the relative errors in the inverse covariance matrix is  $Cond(C) \times \epsilon_{mach}$ , where  $\epsilon_{mach}$  is the computer error,  $\epsilon_{mach} \sim 10^{-16}$  for double precision. Thus the relative error for the inverse matrix coefficients is  $Cond(C) \times \epsilon_{mach} \sim 10^{-4}$  which is almost negligible. We

have also computed the covariance matrix with two independent sets of 5,000 simulations and constrained the best-fitting  $f_{nl}$  of the data with these two matrices. The best-fitting  $f_{nl}$  value of the data is almost the same for both matrices and it agrees with the result obtained with 10,000 simulations suggesting that the convergence is almost reached with 5,000 simulations.

We impose constraints on  $f_{nl}$  through a  $\chi^2$  test. We calculate the expected values of the estimators for different  $f_{nl}$  cases using a set of 300 non-Gaussian simulations. In Fig. 2 we plot the expected values of the 364 statistics  $q_r$  for several  $f_{nl}$  cases for the V+W map. We have checked that the estimator is unbiased. We have evaluated the expected values of the estimator using 200 non-Gaussian simulations of the V+W map and analysed the remaining 100 independent non-Gaussian simulations with  $f_{nl} = 50$ . The result is an average best-fitting  $f_{nl}$  value of 50.6.

In Fig. 3 we plot the values of the statistics for the data map and compare them with the expected values for the best-fitting  $f_{nl}$  model. Then we perform a  $\chi^2$  analysis to find the best-fitting value of  $f_{nl}$  for each map. We also analyse Gaussian simulations in order to obtain the frequentist error bars. Table 2 lists the best-fitting  $f_{nl}$  values for the V+W, Q, V and W combined maps and the main properties of the histograms of the best-fitting  $f_{nl}$  obtained from Gaussian simulations. In the left panel of Fig. 4 we plot the  $\chi^2(f_{nl})$  versus  $f_{nl}$  for the V+W map, and in the right panel of Fig. 4 we plot the histogram of the best-fitting  $f_{nl}$  of 1,000 Gaussian simulations. We have  $-12 < f_{nl} < +86$  for V+W,  $-52 < f_{nl} < +77$  for Q,  $-32 < f_{nl} < +82$  for V and  $+6 < f_{nl} < +123$  for W (all at 95% CL). Note that  $f_{nl}$  increases as the frequency grows from Q to V and W bands. This suggests the possible presence of foregrounds residuals as they are more important at low frequencies and they add a negative contribution to  $f_{nl}$  for the bispectrum estimator (Yadav & Wandelt 2008). To further check if this is also the case for the wavelet estimator, we have also studied the  $K$  and  $Ka$  bands, where the foreground signal has an important contribution. We have obtained  $f_{nl}^K = -497 \pm 42$  and  $f_{nl}^{Ka} = -18 \pm 37$ . Taking this into account and the values of  $f_{nl}$  for the clean and raw Q, V, and W maps (see Tables 2 and 3) we can see that our estimator is sensitive to the presence of foregrounds (biasing the result towards lower values). The sensitivity

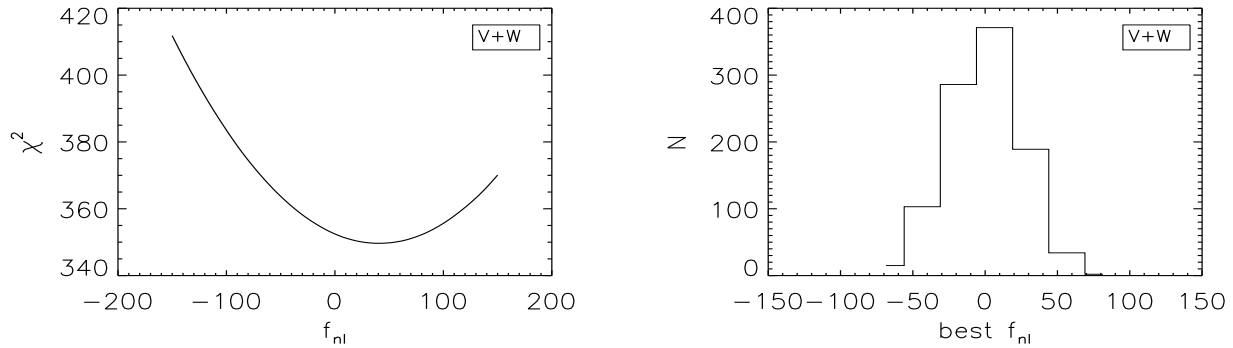


FIG. 4.— The  $\chi^2(f_{nl})$  statistics versus  $f_{nl}$  for the V+W data map and the histogram for the best-fitting  $f_{nl}$  values for a set of 1000 Gaussian V+W simulations. The dispersion is  $\sigma(f_{nl}) = 25$ .

is even more significant for the Q, V, and W bands using the bispectrum (see Table 6 in Komatsu et al. 2009).

It is interesting to point out that the wavelet-based method has an intermediate dimension ( $n_{stat} = 364$  for 12 scales) when compared with the bispectrum combinations ( $\ell_{max}^\beta$  where  $2 < \beta < 3$  and  $\ell_{max} \sim 10^3$ ) and the Minkowski functionals (usually several tens of combinations). The number of wavelet cubic combinations increases significantly with the number of scales.

We also estimate the contribution of the point sources for the V+W combined map as in Curto et al. (2009). We add the point source simulations to the CMB plus noise simulations. For each one of them we compute its best-fitting  $f_{nl}$  and compare it with the obtained for the same case without including the point source simulation. The difference returns an estimate of the contamination on  $f_{nl}$  due to point sources. For the V+W map we have  $\Delta f_{nl} = 6 \pm 5$ . Therefore our estimate taking into account the point sources is  $-18 < f_{nl} < +80$  at 95% CL for the V+W map. Comparing with the best-fitting value for the V+W map given by Yadav & Wandelt (2008),  $f_{nl} = 87$ , our analysis excludes that value at  $\sim 99\%$  CL. However, it is important to point out that Yadav & Wandelt (2008) used different choices for the data maps in the analysis (they used WMAP 3-yr data whereas we use WMAP 5-yr data, different weighting for the channels, etc.), which could also contribute to the found discrepancy. In particular, a simple average of the channels (instead of a noise weighted combination) enhances the signal at high multipoles at the cost of having noisier maps.

### 3.2. Constraints on $f_{nl}$ with the W band

The W map best-fitting  $f_{nl}$  value is only compatible with zero at 99% CL. This result is in apparent discrepancy with the values obtained for the V and V+W maps, which are compatible with zero at 95% CL. The point sources add a low contribution to the W map,  $\Delta f_{nl} = 1 \pm 2$ , and therefore they do not explain its best-fitting value of  $f_{nl} = 65$ . We may wonder if that value can be obtained by a statistical fluctuation. Considering simulations with different models ( $f_{nl} = 0$ ,  $f_{nl} = 40$  and  $f_{nl} = 70$ ) we have confirmed that the best-fitting  $f_{nl}$  for W is compatible with the values obtained for the V and V+W maps.

To understand the relatively large  $f_{nl}$  value found in the W map we have performed some additional tests. First of all, we have checked if this deviation could be

due to the presence of residual foregrounds by studying the V-W map for the clean and the raw (before template subtraction) maps as well as the raw maps for the Q, V, W and V+W cases (see Table 3). We find that there is a very significant (positive) deviation in the clean V-W map. Notice that the V-W map has CMB residuals due to the different resolutions of the V and W bands, which have also been taken into account in the V-W simulations. In any case, the signal due to the CMB is very small and we do not expect it to affect the results given in Table 3 for the different maps. Since this combination contains mainly residual foregrounds and noise, both could be responsible for the deviation. Interestingly, when we repeat the test for the raw V-W map, where foreground contamination should be more important, the best  $f_{nl}$  value becomes compatible with the simulations. This indicates again that foreground emission tends to bias the estimated  $f_{nl}$  towards lower values. This is also observed for the best  $f_{nl}$  value estimated for the raw Q, V, W and V+W maps, which is systematically lower than the one obtained for the clean maps. Therefore, for the case of the raw V-W map, some effect from systematics may be cancelled by foreground residuals.

If foregrounds are not responsible for the deviation found in the W and V-W maps, we may wonder if it is due to systematics present in the W radiometers. To test this possibility, we have studied two different combinations of the four W radiometers, where CMB and foregrounds are basically cancelled. One of these combinations is consistent with Gaussian simulations but the second one shows again a deviation at the 95 per cent CL, indicating the possible presence of some spurious signal in the noise of one or several of the W radiometers. In order to localise further the origin of this signal, we have also studied each W radiometer separately, finding a deviation at the level of 98 per cent for the  $W_2$  radiometer, with a best  $f_{nl}$  value of 91, while the rest of the radiometers are consistent with the zero value at the 95 per cent CL. Finally we have also considered the difference between the two V radiometers, which is found to be compatible with Gaussianity. This further indicates that, if a systematic is responsible of the V-W map, this would be present in the W frequency channel (see Table 3).

All these tests suggest that the relatively large  $f_{nl}$  value obtained for W may come from systematics present

TABLE 3

BEST-FITTING  $f_{nl}$  VALUES FOR DIFFERENT WMAP RADIOMETERS AND COMBINATIONS OF THEM FOR RAW AND CLEAN DATA. WE ALSO PRESENT THE MEAN AND THE DISPERSION OF THE BEST-FITTING  $f_{nl}$  VALUES OBTAINED FROM GAUSSIAN SIMULATIONS.

Map	foreground	best $f_{nl}$	$\langle f_{nl} \rangle$	$\sigma(f_{nl})$
V+W	raw	34	-1	25
Q	raw	-3	0	33
V	raw	16	0	30
W	raw	60	0	30
V-W	raw	-0.02	0.02	0.29
V-W	clean	1.02	0.02	0.29
$W_1$	clean	39	1	41
$W_2$	clean	91	-3	45
$W_3$	clean	23	2	47
$W_4$	clean	59	0	44
$W_1 + W_2 - W_3 - W_4$	clean	-0.52	0.00	0.34
$W_1 - W_2 + W_3 - W_4$	clean	0.85	0.00	0.35
$V_1 - V_2$	clean	-0.01	0.01	0.34

in the W radiometers. In any case, a more exhaustive study is necessary in order to establish the origin of this deviation.

### 3.3. $f_{nl}$ for the North and South hemispheres

The localization property of the wavelets allows a local analysis of the  $f_{nl}$  parameter. In particular, we test the Gaussianity and estimate the best-fitting  $f_{nl}$  value of the V+W combined map using only northern (Galactic latitude  $b > 0$ ) and southern pixels ( $b < 0$ ) in Eq. 2. For both cases the third order statistics obtained for the data are compatible with Gaussian simulations (inside the  $2\sigma$  error bars). In Table 4 we list the best-fitting  $f_{nl}$  values for the northern and southern hemispheres and the main properties of the distribution of the best-fitting  $f_{nl}$  obtained from 1,000 Gaussian simulations. We estimated the contribution of the unresolved point sources as in the previous subsection, and the values are  $\Delta f_{nl} = 7 \pm 7$  for the North and  $\Delta f_{nl} = 5 \pm 7$  for the South. Taking into account this, the results are  $-32 < f_{nl} < 113$  for the North and  $-50 < f_{nl} < 99$  for the South at 95% CL. These values are compatible with zero at 95% CL. We also study the compatibility of the best-fitting value for the North and South hemispheres between them. We compute the difference of the best-fitting  $f_{nl}$  value  $\Delta f_{nl} = f_{nl}^{(N)} - f_{nl}^{(S)}$  for the North and South hemispheres for the set of 1,000 V+W Gaussian simulations. The difference is  $\Delta f_{nl}^{(data)} = 11$  for the data, and for the simulations is  $\Delta f_{nl} = 3 \pm 55$ . The cumulative probability is  $P(\Delta f_{nl} \leq \Delta f_{nl}^{(data)}) = 0.57$  and therefore the difference for the data is compatible with the results obtained from simulations. This means that we do not find any asymmetry in the North-South  $f_{nl}$  value.

## 4. CONCLUSIONS

We have tested the Gaussianity and constrained the  $f_{nl}$  parameter with the 5-yr WMAP data. We use an optimal wavelet-based test. We have considered the V+W, Q, V and W combined maps at high resolution. We have used a set of 300 realistic non-Gaussian simulations and thousands of Gaussian simulations for the analysis. We have computed the wavelet coefficient maps at scales from 6.9 arcmin to 500 arcmin and computed all the

TABLE 4

BEST-FITTING  $f_{nl}$  VALUES OBTAINED FOR THE NORTHERN AND SOUTHERN HEMISPHERES. WE ALSO PRESENT THE MEAN, DISPERSION AND SOME PERCENTILES OF THE DISTRIBUTION OF THE BEST FIT  $f_{nl}$  VALUES OBTAINED FROM GAUSSIAN SIMULATIONS.

Region	best $f_{nl}$	$\langle f_{nl} \rangle$	$\sigma(f_{nl})$	$X_{0.160}$	$X_{0.840}$	$X_{0.025}$	$X_{0.975}$
North	46	2	37	-35	40	-71	74
South	35	-1	38	-39	37	-80	69

possible third order moments (Eq. 2) using appropriate extended masks.

The data are compatible with Gaussian simulations for the considered combined maps (see Table 1). We have imposed constraints on the non-linear coupling parameter  $f_{nl}$  by using non-Gaussian simulations with  $f_{nl}$ . The results show that  $f_{nl}$  increases when we go from the Q to the V and W combined maps. This frequency dependence also appears in the results by Yadav & Wandelt (2008); Komatsu et al. (2009); Curto et al. (2009). The results are compatible with zero at 95% CL for the V+W, Q, and V combined maps, but not for the W map (which is compatible at 99% CL). This value cannot be explained by unresolved point sources since their contribution is  $\Delta f_{nl} = 1 \pm 2$  for the W map. We have estimated the probability of having those values with simulations and the results do not show incompatibility among different channels. We have also seen that the relatively large  $f_{nl}$  value obtained for the W band may come from systematics in one or several radiometers of this band.

We have also estimated the contribution of unresolved point sources to  $f_{nl}$  for the V+W map using a realistic model given by de Zotti et al. (2005). The results are  $\Delta f_{nl} = 6 \pm 5$ . Taking into account this value, our best estimate for  $f_{nl}$  is  $-18 < f_{nl} < +80$  at 95% CL. The use of new scales and all the possible third order moments has returned better constraints to  $f_{nl}$  and lower error bars compared with the results by Curto et al. (2009) and previous works. Our best estimate is compatible with the values obtained by Komatsu et al. (2009) and it excludes the best-fitting  $f_{nl}$  value obtained by Yadav & Wandelt (2008) at the  $\sim 99\%$  CL.

Finally we have constrained  $f_{nl}$  for the North and South hemispheres and the results give two best-fitting values that are compatible with zero at 95% CL and also are compatible between them. Therefore we do not find any North-South asymmetry for this parameter.

## ACKNOWLEDGMENTS

We are thankful to Frode Hansen, Michele Liguori and Sabino Matarrese for supplying maps with primordial non-Gaussianity. The authors thank J. González-Nuevo for providing the  $dN/dS$  counts and for his useful comments on unresolved point sources. The authors thank P. Vielva, E. Komatsu and M. Cruz for useful discussions. We also thank R. Marco and L. Cabellos for computational support. We acknowledge partial financial support from the Spanish Ministerio de Ciencia e Innovación project AYA2007-68058-C03-02. A. C. thanks the Spanish Ministerio de Ciencia e Innovación for a pre-doctoral fellowship. The authors acknowledge the computer resources, technical expertise and assistance provided by the Spanish Supercomputing Network (RES) node at Universidad de Cantabria. We acknowledge the use of

Legacy Archive for Microwave Background Data Analysis (LAMBDA). Support for it is provided by the NASA

Office of Space Science. The HEALPix package was used throughout the data analysis (Górski et al. 2005).

## REFERENCES

- Albrecht, A. & Steinhardt, P. J. 1982, *Physical Review Letters*, 48, 1220
- Bartolo, N., Komatsu, E., Matarrese, S., & Riotto, A. 2004, *Phys. Rep.*, 402, 103
- Bennett, C. L., Hill, R. S., Hinshaw, G., Nolta, M. R., Odegard, N., Page, L., Spergel, D. N., Weiland, J. L., Wright, E. L., Halpern, M., Jarosik, N., Kogut, A., Limon, M., Meyer, S. S., Tucker, G. S., & Wollack, E. 2003, *ApJS*, 148, 97
- Cabella, P., Liguori, M., Hansen, F. K., Marinucci, D., Matarrese, S., Moscardini, L., & Vittorio, N. 2005, *MNRAS*, 358, 684
- Cayón, L., Martínez-González, E., Argüeso, F., Banday, A. J., & Górski, K. M. 2003, *MNRAS*, 339, 1189
- Cremineilli, P., Nicolis, A., Senatore, L., Tegmark, M., & Zaldarriaga, M. 2006, *Journal of Cosmology and Astro-Particle Physics*, 5, 4
- Cremineilli, P., Senatore, L., Zaldarriaga, M., & Tegmark, M. 2007, *Journal of Cosmology and Astro-Particle Physics*, 3, 5
- Curto, A., Aumont, J., Macías-Pérez, J. F., Martínez-González, E., Barreiro, R. B., Santos, D., Désert, F. X., & Tristram, M. 2007, *A&A*, 474, 23
- Curto, A., Macías-Pérez, J. F., Martínez-González, E., Barreiro, R. B., Santos, D., Hansen, F. K., Liguori, M., & Matarrese, S. 2008, *A&A*, 486, 383
- Curto, A., Martínez-González, E., Mukherjee, P., Barreiro, R. B., Hansen, F. K., Liguori, M., & Matarrese, S. 2009, *MNRAS*, 393, 615
- De Troia, G., Ade, P. A. R., Bock, J. J., Bond, J. R., Borrill, J., Boscaleri, A., Cabella, P., Contaldi, C. R., & et al. 2007, *ApJL*, 670, L73
- de Zotti, G., Ricci, R., Mesa, D., Silva, L., Mazzotta, P., Toffolatti, L., & González-Nuevo, J. 2005, *A&A*, 431, 893
- Gangui, A., Lucchin, F., Matarrese, S., & Mollerach, S. 1994, *ApJ*, 430, 447
- Górski, K. M., Hivon, E., Banday, A. J., Wandelt, B. D., Hansen, F. K., Reinecke, M., & Bartelmann, M. 2005, *ApJ*, 622, 759
- Gott, J. R., Colley, W. N., Park, C.-G., Park, C., & Mugnolo, C. 2007, *MNRAS*, 377, 1668
- Guth, A. H. 1981, *Phys. Rev. D*, 23, 347
- Hikage, C., Matsubara, T., Coles, P., Liguori, M., Hansen, F. K., & Matarrese, S. 2008, *MNRAS*, 389, 1439
- Komatsu, E., Dunkley, J., Nolta, M. R., Bennett, C. L., Gold, B., Hinshaw, G., Jarosik, N., Larson, D., Limon, M., Page, L., Spergel, D. N., Halpern, M., Hill, R. S., Kogut, A., Meyer, S. S., Tucker, G. S., Weiland, J. L., Wollack, E., & Wright, E. L. 2009, *ApJS*, 180, 330
- Komatsu, E., Kogut, A., Nolta, M. R., Bennett, C. L., Halpern, M., Hinshaw, G., Jarosik, N., Limon, M., Meyer, S. S., Page, L., Spergel, D. N., Tucker, G. S., Verde, L., Wollack, E., & Wright, E. L. 2003, *ApJS*, 148, 119
- Komatsu, E. & Spergel, D. N. 2001, *Phys. Rev. D*, 63, 063002
- Komatsu, E., Wandelt, B. D., Spergel, D. N., Banday, A. J., & Górski, K. M. 2002, *ApJ*, 566, 19
- Liguori, M., Matarrese, S., & Moscardini, L. 2003, *ApJ*, 597, 57
- Liguori, M., Yadav, A., Hansen, F. K., Komatsu, E., Matarrese, S., & Wandelt, B. 2007, *Phys. Rev. D*, 76, 105016
- Linde, A. D. 1982, *Physics Letters B*, 108, 389
- . 1983, *Physics Letters B*, 129, 177
- Martínez-González, E. 2008, (arXiv:0805.4157)
- Martínez-González, E., Gallegos, J. E., Argüeso, F., Cayón, L., & Sanz, J. L. 2002, *MNRAS*, 336, 22
- Mukherjee, P. & Wang, Y. 2004, *ApJ*, 613, 51
- Pietrobon, D., Cabella, P., Balbi, A., de Gasperis, G., & Vittorio, N. 2009, *MNRAS*, 396, 1682
- Rudjord, Ø., Hansen, F. K., Lan, X., Liguori, M., Marinucci, D., & Matarrese, S. 2009, *ApJ*, 701, 369
- Salopek, D. S. & Bond, J. R. 1990, *Phys. Rev. D*, 42, 3936
- Santos, M. G., Heavens, A., Balbi, A., Borrill, J., Ferreira, P. G., Hanany, S., Jaffe, A. H., Lee, A. T., Rabii, B., Richards, P. L., Smoot, G. F., Stompor, R., Winant, C. D., & Wu, J. H. P. 2003, *MNRAS*, 341, 623
- Slosar, A., Hirata, C., Seljak, U., Ho, S., & Padmanabhan, N. 2008, *Journal of Cosmology and Astro-Particle Physics*, 8, 31
- Smith, K. M., Senatore, L., & Zaldarriaga, M. 2009, *Journal of Cosmology and Astro-Particle Physics*, 9, 6
- Spergel, D. N., Bean, R., Doré, O., Nolta, M. R., Bennett, C. L., Dunkley, J., Hinshaw, G., Jarosik, N., & et al. 2007, *ApJS*, 170, 377
- Verde, L., Wang, L., Heavens, A. F., & Kamionkowski, M. 2000, *MNRAS*, 313, 141
- Vielva, P. & Sanz, J. L. 2009, *MNRAS*, 397, 837
- Yadav, A. P. S. & Wandelt, B. D. 2008, *Physical Review Letters*, 100, 181301